

# Automatic Detection of Bone Metastasis in Vertebrae by Using CT Images

Sheng-Fang Huang, and Kuo-Hsien Chiang

**Abstract**—Commonly diagnosed in advanced breast cancer patients, especially in vertebrae, bone metastases can appear lytic, sclerotic, or anywhere in between these extremes. Given its ability to alter the therapeutic strategy, bone metastases is a critical issue in staging and follow-up of breast cancer. This work presents a novel computer-aided diagnosis (CAD) system to detect metastasis in vertebrae by using whole body computed tomography (CT). An automated method is developed to extract ROIs of trabecular centrum from vertebrae. Eleven texture features and their inter-slice differences are then calculated for each ROI. Next, total 33 features are fed into an artificial neural network (ANN) to determine whether any abnormality occurs in the trabecular centrum. The datasets include 35 breast cancer patients who underwent a whole-body PET/CT scan between 2007 and 2011. The average sensitivity, specificity, and accuracy are 85.4%, 91.8%, and 89.7%, respectively. Capable of identifying possible bone lesions by using CT images, the proposed CAD system can incorporate with features of nuclear medicine images to increase diagnostic accuracy in an automated CAD system for estimating bone metastases quantitatively.

**Index Terms**—X-ray imaging, Computed Tomography, Spine, Computer-Aided Diagnosis, Neural Network

## I. INTRODUCTION

As bone is the most common site of distant metastasis, metastases to bone are diagnosed in 30-85% of advanced breast cancer patients [1]. Bone metastases have important implications in terms of worsening morbidity and mortality of patients. The vertebral column is the most frequent site of metastatic involvement of the skeleton [2]. Bone metastases are characterized as either osteolytic (lytic) or osteoblastic, in which some patients can have both types (Fig 1). Whereas bone resorption predominates, little new bone formation and focal bone destruction occurs, giving the lesions an osteolytic appearance. Conversely, lesions appear to be sclerotic if bone metastases are formed by increasing osteoblastic activity. Bone metastasis complications include bone pain, pathological fractures, hypercalcemia, and spinal cord compression [3, 4]. Capable of altering therapeutic strategy, bone metastases is a priority concern in the initial staging and follow-up of breast cancer.

Manuscript received March 18, 2012; revised March 31, 2012. This work was financially supported in part by the National Science Council of Taiwan under Grant NSC 100-2221-E-320-007.

S.-F. Huang is with Department of Medical Informatic Tzu Chi University, Hualien 970, Taiwan (phone: 886-3-8656301~2388; fax: 886-3-8579409; e-mail:SFHuang@mail.tcu.edu.tw).

K.-H. Chiang is with Department of Radiology Buddhist Tzu Chi General Hospital, Hualien 970, Taiwan (e-mail: spider.beef@gmail.com).

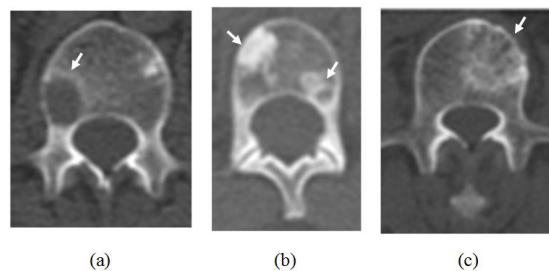


Fig. 1. Metastatic lesions in vertebrae can be (a) osteolytic, (b) osteoblastic, or (c) mixed.

Widely prescribed to search for bone metastases, bone scintigraphy permits a whole-body examination with a relatively high sensitivity [5, 6]. Tracer accumulates in the reactive new bone that is formed in response to the lesion. However, increased bone metabolic rates can be owing to cancer unrelated conditions such as fractures, arthritis, or infections [7-9]. Therefore, sensitivity and specificity are limited [10-12]. On the other hand, although superior to bone scintigraphy in terms of detecting bone metastases [5, 13-15]. FDG-PET may yield a high false-positive rate in abnormalities with rapid glucose metabolism, such as acute osteomyelitis and fractures. Therefore, images should be carefully interpreted when considering symptoms and clinical findings [16, 17]. Previous studies have also demonstrated a low detection rate of osteoblastic metastases from prostate and breast cancer by using FDG-PET [15, 18-20]. Fused PET/CT scanners integrate the functional data of PET with the detailed anatomical information of CT scanners in single examination, leading to the development of a new modality available for whole-body imaging. Capable of providing visceral organs and lymph nodes, as well as excellent skeletal details, CT images have a high sensitivity for diagnosing bone metastases, ranging from 71% to 100% [9, 21, 22]. Malignancy can be diagnosed in locations with lytic, sclerotic, and mixed lytic-sclerotic changes in CT images. Multidetector CT (MDCT) can be an alternative method for whole body bone screening to perform skeletal scintigraphy [23]. MDCT scanners achieve thin collimation and fast scanning, yielding a significantly improved scanning resolution and a sequence of thin-sliced images. However, given the normally time consuming task of radiologists in interpreting hundreds of CT slices, computer-aided diagnosis (CAD) systems for bone metastasis may increase the reliability of bone metastasis screening.

The most complex aspect of CAD applications involves the synthesis of imaging information from the extracted target organ or ROI to make a diagnosis. Many semi-automatic or

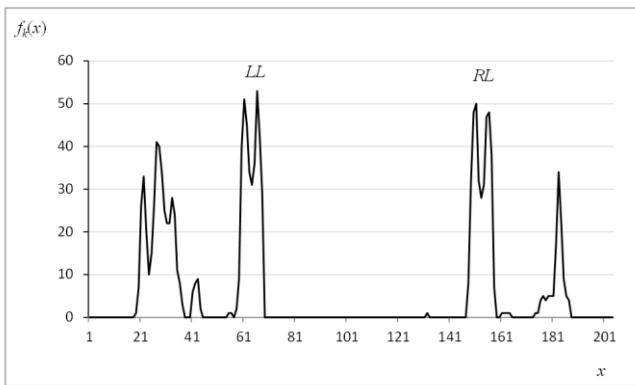


Fig. 2. The value of  $f_k(x)$  denotes the accumulation of the horizontal counts of non-zero pixels at some  $x$  from the bottom to the  $k$ -th image plane. In this example,  $k$  was 258 where there were 263 image planes in total. The markers  $LL$  and  $RL$  respectively correspond to the spatial locations for the left and right legs.

automatic segmentation methods have been developed for the recognition of vertebrae. However, to our knowledge, a limited number of articles describe diagnosis systems for bone metastases. O'Conner et al. [24] developed a detection method for lytic bone metastasis by using regular CT images. Based on a dynamic graph search, that study traced the spinal cord from thoracic spine to lumbar spine to establish a local spine coordinate system. Potential lytic bone lesions were also detected using a watershed algorithm. A set of 26 quantitative features were computed for each region candidate. Moreover, whether a candidate is a true lesion was determined using support vector machines (SVM). In sum, none of the above methods are fully automated or can be used in both blastic and lytic metastases.

This work presents a completely automated CAD system to detect vertebral metastasis of breast cancer by using whole body CT images. An image segmentation method was developed to determine the region of interest (ROI) of trabecular centrum for each slice. Because the cortical shell of vertebral body displays a similar high intensity of blastic metastasis, isolating the shell can increase the classification accuracy. For each ROI, 33 texture features are then calculated, including 11 texture features and 22 inter-slice features of these textures. Finally, whether an abnormality occurs in the trabecular centrum is determined by feeding all of the features into a multilayer perceptron (MLP) neural network to identify. The results are compared with those of manual classification as validation of the proposed CAD method. Importantly, the proposed method provides a high diagnostic prediction accuracy and to increase interpretive efficiency for radiologists.

## II. DATA ACQUISITION

CT images were obtained by using a combined PET/CT scanner (Discovery LS; GE Medical Systems, Waukesha, Wis) in whole-body PET scanning. Scanning was performed from head to upper thigh regions for 40 minutes after intravenously administering 400 MBq of  $^{18}\text{F}$ -fluoride by using a Discovery LS PET/CT system (GE Medical Systems). The datasets include 35 patients (39–78 years old; mean age of 52.3 years old) with breast cancer who had a whole-body PET/CT scan

between 2007 and 2011. Patients had between zero and 17 metastatic vertebrae (average of 5.5). This study excluded patients with severe degenerative disease of spine or hardware such as cement, rods, or screws. For all of the patients, CT images were reviewed by an experienced radiologist. Each vertebra was assessed using a binary system in which a score of 1 indicated definite positive for vertebral metastasis and 0 indicated negative. Totally, 4,413 CT images were obtained among the 35 patients, included in 192 metastatic vertebrae and 392 normal vertebrae. This study was approved by the local ethics committee, and the informed consent was wavered obtained from all included patients.

## III. ROI EXTRACTION METHOD

### A. Preprocessing

The source images were initially resized from  $512 \times 512$  to  $204 \times 204$  pixels and then, transformed to a gray level image using a window center of 100 and a window width of 300 to highlight the bone regions. The image was then converted into a binary data by using a threshold  $T$  was then used to convert the image into binary data, where the pixels with value larger than  $T$  were labeled 1 to denote as bone region. The value of  $T$  was adaptively determined using Ostu's method [25].

### B. Bounding Box Computation

#### Locating Pelvis

Starting from the bottom in the volumetric stack of all of the binary images, this method accumulated the horizontal counts of non-zero pixels to the  $k$ -th image slice, which can be denoted by a function  $f_k(x)$  for horizontal coordinate  $x$ . A normal individual has a typical curve of  $f_k(x)$  as illustrated in Fig. 3, where the hills from left to right correspond to left hand, left leg, right leg, and right hand, respectively. The two classes can be separated using a threshold obtained by the binarization method [25]. For each class, the same method can be performed again to separate the hand and the leg, eventually resulting in four sub-classes.

The spatial locations for the left and right legs, denoted as  $LL$  and  $RL$  respectively, can be obtained as reference landmarks by computing the averages for the middle two sub-classes. Furthermore, the non-zero pixel counts around the middle point between  $LL$  and  $RR$ , denoted as  $mp$ , starts to increase as the accumulation proceeds to the pelvis. Assume there are  $n$  CT image planes for a scan. The anatomical landmark  $PELVIS$  can thus be estimated according to the following formula:

$$PELVIS = \max \left\{ k \mid \sum_{a \leq x \leq b} f_k(x) > \min[f_k(LL), f_k(RL)] \right\} \text{ for } k = n-1, \dots, 1, 0 \quad (1)$$

where  $[a, b] = [(LL + mp) / 2, (mp + RL) / 2]$ . The scope formed by the estimated reference landmarks  $LL$ ,  $LR$ , and the pixels of limbs were excluded by using  $PELVIS$ .

#### Spine Localization Using Bone Diagram

A spatial image map for spine was formed by averaging the value for each pixel over all of the input images. The range of the vertebral column can therefore be statistically revealed on this average image. Pixels with their values exceeding 50 were selected and then, grouped into regions. A bounding box

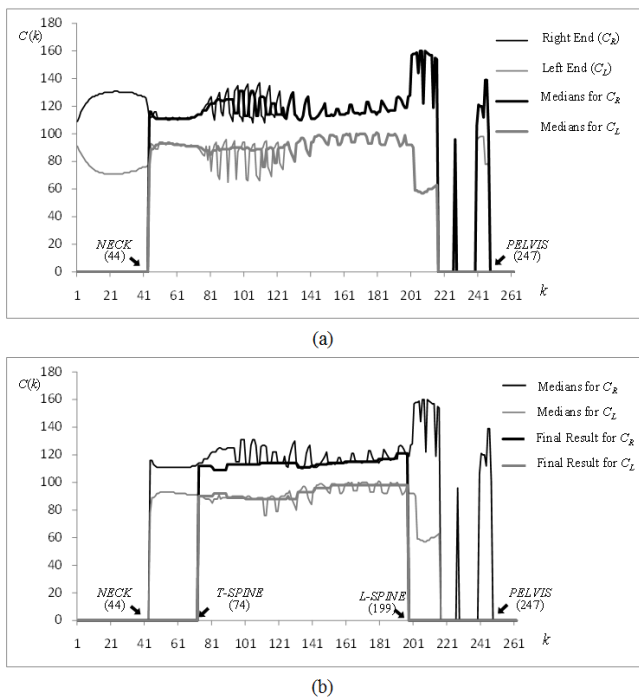


Fig. 3. (a) An example of bone diagram. The two thin solid curves, denoted as  $C_L$  and  $C_R$ , respectively indicate the leftmost and rightmost ends for spinal bones. The thick curves show the outcome of median filtering on  $C_L$  and  $C_R$  from the reference landmark NECK to PELVIS. (b) The thick curves denote the computed results of bounding boxes for the extracted spine from thoracic spine (T-SPINE) to lumbar spine (L-SPINE).

for the largest region was determined as a reference window not only to exclude the bones not connected to the spine, but also to generate a bone diagram. In each binary image  $I_k$ , a region with its center not contained in this window was removed. Next, the leftmost and rightmost ends of the remaining connected components were plotted individually in a diagram, where the horizontal axis refers to the number of the image plane, and the vertical axis denotes the leftmost and rightmost coordinates of the region on a given  $k$ -th slice. Figure 3(a) displays a typical bone diagram. The two thin solid curves, denoted as  $C_L(k)$  and  $C_R(k)$ , represent the leftmost and rightmost ends of the spinal bones, respectively.

The upper thoracic spine was located by starting from I0 and then examining each binary image  $I_k$  along the z-axis. During the iterative process, the horizontal width of the connected components, which is equivalent to  $(C_R(k) - C_L(k))$ , was computed. Simultaneously, the maximum and minimum widths were updated. Since the width for the middle neck is relatively smaller than that of the head, the position was denoted here as NECK at the image level, where the scanned width was less than 60% of the maximum width. Below the level of NECK, the process was continued to locate a reference landmark where the width was 60% larger than the minimum width, denoted here as T-SPINE.

Next, local median values for the curve  $C_L(k)$  and  $C_R(k)$  were estimated to remove the rib-cage, as shown in the two thick solid curves in Fig. 3(a). Based on the experiments, the kernel size for local computation was set to 5. Second, the bones connected to vertebral joints were isolated by grouping the images from T-SPINE to PELVIS into  $M$  sections. For each section, a spatial image map was generated and its bounding box, defined as  $B_v$ , was computed as a local

reference window. For each binary image  $I_k$  where  $v \leq k/M < v+1$ , a non-zero pixel was set to 0 if it was not included in  $B_v$ . The bounding box for the connected components on each slice was calculated. The bone diagram was also regenerated to reflect this modification, as shown in Fig. 3(b). Here, the value of  $M$  was 10. The position of lumbar spine was determined at position  $x$  where  $(C_R(k) - C_L(k))$  was twice larger than the mean width, which we denoted as L-SPINE. Finally, a set of sub-images were then defined from the reference landmark T-SPINE to L-SPINE in the original CT images according to these bounding boxes, which were later used as an input to detect the spinal canal and vertebral body.

### Skeletal Structure Differentiation

Detecting and localizing spinal canal (SC) are necessary to facilitate the analysis of spinal structures. The sub-image was extracted according to the bounding boxes described in the previous section. Mean filtering was then performed with a kernel size of 5 to reduce the noise effect, followed by histogram equalization to increase the contrast. Next, the image was transformed to a binary image by using an adaptively computed threshold  $T_k$ . Finally, the binary image, denoted as  $M_k(x)$ , was used as an image mask to represent the profile of skeletal regions. Since the SC profile and the spine have the same medial axis, for each  $M_k(x)$  with a size equal to  $H_k \times W_k$ , a sliding window with a size of  $W_k$  is used to scan in a horizontal direction. In the window, the vertical distance between the uppermost and the lowermost non-zero pixels was computed, denoted by  $D_k(j)$  where  $1 \leq j \leq W_k - 1$ . The horizontal coordinate of the largest distance,  $j_{med}$ , was defined as the medial axis.

Next, a  $15 \times 15$  mask on the image of  $G_k(x)$  was used to search for each pixel along the medial axis from the positions at  $0.25H_k$  to  $0.75H_k$  to find the vertical coordinate for SC. For each point, the intensities in the mask were summed up. The point  $s_k$  was defined as an initial estimate for the center point of SC in the  $k$ -th image slice if it has the minimum sum. By linking all  $s_k$ , a path representing the middle line for SC can be obtained.

Centered at  $s_k$ , the information of SC contour on the  $k$ -th image slice can be represented by its signature. The signature of a contour is a 1-D function that describes the distance from the center to its boundary on a specific angle  $\theta$ . Assume that  $d(m, n)$  denotes the Euclidean distance between two points  $m$  and  $n$ , and  $\rho(m)$  represents the angle of the point  $m$  respective to the center. In the proposed approach, the signature of the SC contour on the  $k$ -th image slice can be defined as follows.

$$r(\theta) = \min_u \{d(u, s'_k) | d(u, s'_k) > 0, \rho(u) = \theta \text{ and } I_k(u) > T_k\} \quad (2)$$

Next, a median filtering and a mean filtering with a kernel size of  $23^\circ$  were successively applied to generate a smooth contour for the SC.

To extract the trabecular centrum, the part upper to the computed SC area in the ROI of the image was chosen as an initial bounding box for the trabecular centrum. In the bounding box, the candidate pixels were selected if their intensities exceeded a threshold equal to  $T_k/2$ . The threshold

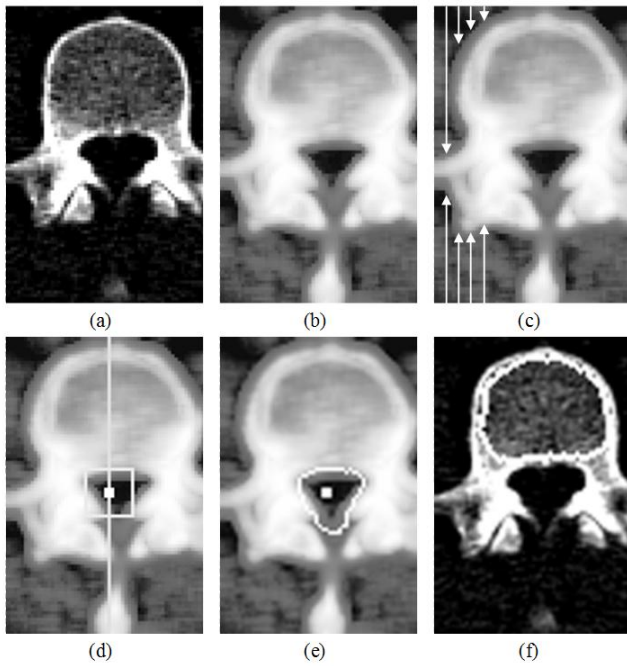


Fig. 4. The procedures of the contour extraction for spinal canal and trabecular centrum. (a) Original image (window center of 300 with width 50). (b) The outcome obtained by image enhancement. (c) The vertical distance of the vertebrae was scanned for locating the medial line. (d) Along the medial line, a mask was used for finding the center of spinal canal. (e) The contour of spinal canal computed using signature. (f) The final result for trabecular centrum extraction (merged with (a)).

was decreased to half in order to recruit more candidate pixels of bone including the lesion part. For the  $k$ -th image slice, the spatial gravity for these pixels, denoted as  $b_k$ , was calculated to be the center of vertebral body. Next, the contour was estimated using the same procedure similar to that in Equation (3). The signature for the contour of trabecular centrum can be defined as follows.

$$r_b(\theta) = \max_u \{d(u, b_k) | d(u, s'_k) > 0, \rho(u) = \theta \text{ and } I_k(u) > T_k / 2\} \quad (3)$$

The average value and standard deviation of  $r_b(\theta)$  were again used to remove the outliers. The boundary was smoothed using median filtering and mean filtering. The region enclosed by  $r_b(\theta)$  was defined as the ROI of trabecular centrum. Figure 4 illustrates the segmentation procedures.

#### IV. TEXTURE ANALYSIS

In this work, Haralick texture features were used to differentiate between normal trabecular centrum and metastasis [26]. Haralick features are derived from the gray-level co-occurrence matrix. If there are  $N_g$  gray levels, then the dimension of the co-occurrence matrix is  $N_g \times N_g$ . The nine Haralick texture features can be calculated directly using the equations listed in Table I. In this table,  $P(i, j)$  denotes the entry of the gray-level co-occurrence matrix at  $(i, j)$ , and  $\mu$  is the mean values for all  $P(i, j)$ . The averages and standard deviations for the two dimensions are represented by  $\mu_x, \mu_y, \sigma_x$ , and  $\sigma_y$ .

A window center of 500 and a window width of 1000 were used to enhance the inner tissues of trabecular centrum contained in the ROIs. Eleven texture features were computed

Property	Equations
Angular Second Moment	$f_1 = \sum_{i=0}^{N_g-1} \sum_{j=0}^{N_g-1} \{P(i, j)\}^2$
Contrast	$f_2 = \sum_{k=0}^{N_g-1} k^2 \{ \sum_{i=1}^{N_g} \sum_{j=1}^{N_g} P(i, j) \},  i-j =k$
Correlation	$f_3 = \frac{\sum_{i=0}^{N_g-1} \sum_{j=0}^{N_g-1} (ij)P(i, j) - \mu_x \mu_y}{\sigma_x \sigma_y}$
Inverse Difference Moment	$f_4 = \sum_{i=0}^{N_g-1} \sum_{j=0}^{N_g-1} \frac{P(i, j)}{1+(i-j)^2}$
Entropy	$f_5 = \sum_{i=0}^{N_g-1} \sum_{j=0}^{N_g-1} (P(i, j) \log P(i, j))$
Cluster Shade	$f_6 = \sum_{i=1}^{N_g-1} \sum_{j=1}^{N_g-1} (i+j-\mu_x-\mu_y)^3 P(i, j)$
Cluster Prominence	$f_7 = \sum_{i=0}^{N_g-1} \sum_{j=0}^{N_g-1} (i+j-\mu_x-\mu_y)^4 P(i, j)$
Homogeneity	$f_8 = \sum_{i=0}^{N_g-1} \sum_{j=0}^{N_g-1} \frac{P(i, j)}{1+ i-j }$
Variance	$f_9 = \sum_{i=0}^{N_g-1} \sum_{j=0}^{N_g-1} ((i-\mu)^2 P(i, j))$

for each ROI, including nine Haralick textures and two local statistical features, mean and standard deviation. Their feasibility was then evaluated by using the unpaired Student's t-test (two-tailed); in addition, the features that have  $p$ -value under 0.01 were preserved. Some false positive lesions in the classification could be observed near the upper and lower endplates. Partial inclusion of the vertebral endplates may lead to incorrect classification as blastic tumor tissue. Therefore, in this work, a three-dimensional (3D) consistency check is performed based on depth information. To reduce errors caused by a false-negative, two differences with the previous and the next slices were computed for each of the 11 texture features, subsequently producing 22 additional features.

#### V. CLASSIFICATION

This work also attempted to determine whether a ROI is a normal trabecular centrum or contain metastasis by adopting a general MLP neural network and chose the back-propagation algorithm as the learning rule. Values derived by the output node of the neural network are either 0 or 1, respectively representing whether a pixel belongs to normal or abnormal tissues. Here, three-layer back-propagation algorithms was used. The first layer was an input layer including 33 neurons (nodes) that denote the foregoing 33 features extracted from a specific ROI. The framework of this neural network consisted of a hidden layer with 18 neurons. The last layer was the output layer with two neurons which classifies the ROI. An attempt was made to stabilize this neural network by training the data with 500 iterations. The learning parameter was set to 0.01 and the momentum was chosen as 0.01 for quick convergence.

The accuracy of feature classification was estimated using

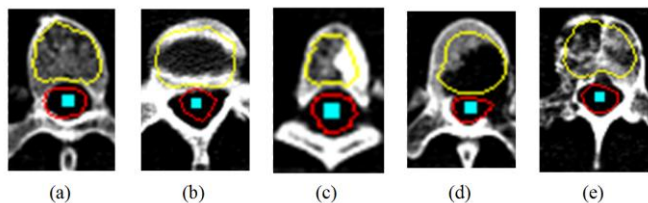


Fig. 5. Segmentation and prediction result of normal and metastatic trabecular centrum. (a) normal trabecular centrum classified as normal. (b) intervertebral disc and endplates classified as normal. (c) osteoblastic lesion, classified as metastasis. (d) osteolytic lesion, classified as metastasis. (e) mixed lesion, classified as metastasis.

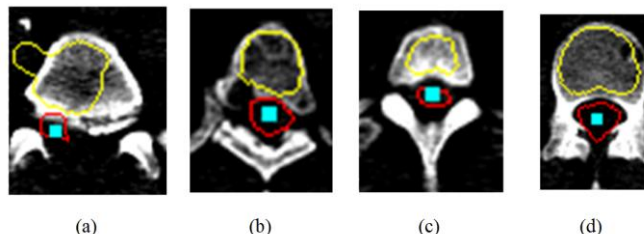


Fig. 6. Examples of erroneous segmentation results. (a) False-positive result due to incorrect segmentation. (b) False-negative result due to incorrect ROI segmentation, which excluded the lesion. (c) False-positive result due to partial inclusion of endplates. (d) False-negative result because the lesion is too small.

the  $k$ -fold cross-validation method. With the  $k$ -fold cross-validation method, the 35 cases were randomly divided into  $k$  groups. The first group was chosen as the test set, and the remaining  $(k-1)$  groups were used as the train set to train the neural network. The process was repeated until every group had been tested. Each time a group was to be tested, the other  $(k-1)$  groups were used to train the network first. Here,  $k$  was 5. The pixels recognized as abnormal were grouped into regions and compared with the ROIs manually segmented by an experienced physician (one of the authors). If the proposed CAD system detects any region in common with a manual detection, it was considered a true detection of liver lesion; otherwise, it was considered a false detection. If more than one CAD detections corresponded to a single lesion of reference-standard detection, the detections were still counted them as a true-positive (TP) finding.

## VI. RESULTS

Features from ROIs of 4413 slices were extracted, including in 192 metastatic vertebrae and 392 normal vertebrae of 35 patients. Table II summarizes the prediction results using 11 basis features without inter-slice information. The sensitivity was 79.2%, the specificity was 90.3%, and the accuracy was 86.6%.

By using the other 22 inter-slice features formed by the differences for each of the 11 texture features, the FN can be significantly decreased from 20.8% to 14.6%. Finally, the average sensitivity, specificity, and accuracy were 85.4%, 91.8% and 89.7%. Table III summarizes prediction results with the total 33 features. Figure 5 describes experimental results for different vertebra types. Accordingly, the proposed system can successfully extract the ROIs for normal and metastatic trabecular centrum, resulting in an accurate classification.

TABLE II  
PREDICTION WITHOUT INTER-SLICE FEATURES

	Normal vertebra	Abnormal vertebra
Negative Prediction	354 TN	40 FN
Positive Prediction	38 FP	152 TP
Total	392	192

TP: True Positive, TN: True Negative, FP: False Positive, FN: False Negative.

TABLE III  
PREDICTION WITH THE TOTAL 33 FEATURES INCLUDING INTER-SLICE INFORMATION

	Normal vertebra	Abnormal vertebra
Negative Prediction	360 TN	28 FN
Positive Prediction	32 FP	164 TP
Total	392	192

TP: True Positive, TN: True Negative, FP: False Positive, FN: False Negative.

## VII. DISCUSSION

Although CT is not the optimum modality for screening of bone metastases, CT images can identify most bone metastases. Detecting vertebral metastases using a computer is a challenging task, owing to the variation in bone attenuation within and among patients, as well as to the diversity of non-metastatic abnormalities such as degenerative disk disease. O'Conner et al. [10] developed a method based on watershed segmentation algorithm and SVM for lytic bone metastasis detection by using regular CT images of 50 patients. The sensitivity was 0.94, while the false-positive was 4.5 per patient. This work developed a neural network based CAD system to diagnose vertebral metastasis in breast cancer patients by using whole-body CT images. The average sensitivity, specificity, and accuracy were 85.4%, 91.8% and 89.7%. In contrast to O'Conner et al., the false-positive was only 0.9 per patient. The proposed CAD system provides an automated method for both kinds of metastases with a high sensitivity and specificity.

Despite its merits, the proposed method has certain limitations. This work excluded studies involving hardware such as cement, rods, or screws, owing to the possible confounding effects of the artifacts produced by the devices. Furthermore, a faulty contour in the trabecular centrum segmentation could lead to erroneous diagnostic results, as shown in Fig. 6. In Fig. 6(a), the incorrect positioning of SC and the outlier region at the upper-left corner led an erroneous segmentation for trabecular centrum; therefore, the dark background included in the ROI was classified inaccurately as a lesion. Conversely, the example in Fig. 6(b) obtained a false-negative result since the ROI excluded the lesion because the lytic metastasis dropped out of the boundary of vertebrae. Furthermore, partial inclusion of endplates and a small lesion could affect the accuracy (Figs. 6(c) and (d)).

Most errors in the classification were found near the upper and lower end plates. Endplates containing high intensity pixels, partial inclusion of the vertebral endplates might be incorrectly classified as a blastic tumor tissue. Consider a 3-D consistency check using inter-slice differences. The accuracy

was increased from 86.6% to 89.7% while the FN rate was significantly decreased from 20.8% to 14.6%. Additionally, the proposed CAD system may fail to detect a small tumor.

### VIII. CONCLUSION

In conclusion, this work has described a novel CAD method capable of detecting both lytic and blastic metastases in the thoracolumbar spine. Efforts are underway in our laboratory to incorporate features computed from PET images into the proposed method to increase diagnostic accuracy in an automated CAD system for quantitatively estimating bone metastases. Future research should also refine the proposed segmentation method so that it can extract the profile of trabecular centrum accurately and remove the parts of intervertebral disc and endplates. Additionally, a model-based method should also be adopted not only to solve the segmentation problem when the vertebrae shape is distorted by lesions or spurs, but also to locate intervertebral discs. Moreover, since metastasis can occur in all bones, a more complex procedure is necessary to perform bone division for the entire body in order to detect all possible lesions.

### REFERENCES

[1] E. F. Solomayer, I. J. Diel, G. C. Meyberg, C. Gollan, and G. Bastert, "Metastatic breast cancer: clinical course, prognosis and therapy related to the first site of metastasis," *Breast Cancer Res. Tr.*, vol. 59, no. 3, pp. 271-278, Feb. 2000.

[2] D. A. Wong, V. L. Fornasier, and I. MacNab, "Spinal metastases: the obvious, the occult, and the impostors," *Spine*, vol. 15, no. 1, pp. 1-4, Jan 1990.

[3] G. D. Roodman, "Biology of osteoclast activation in cancer," *J. Clin. Oncol.*, vol. 19, no. 15, pp. 3562-3571, Aug 1 2001.

[4] R. D. Rubens, "Bone metastases-The clinical problem," *Eur. J. Cancer*, vol. 34, no. 2, pp. 210-213, Feb. 1998.

[5] T. Bury, A. Barreto, F. Daenen, N. Barthelemy, B. Ghaye, and P. Rigo, "Fluorine-18 deoxyglucose positron emission tomography for the detection of bone metastases in patients with non-small cell lung cancer," *Eur. J. Nucl. Med. Mol. I.*, vol. 25, no. 9, pp. 1244-1247, Sep 1998.

[6] M. V. Merrick, "Review article-Bone scanning," *Brit. J. Radiol.*, vol. 48, no. 569, pp. 327-351, May 1975.

[7] L. D. Rybak and D. I. Rosenthal, "Radiological imaging for the diagnosis of bone metastases," *Q. J. Nucl. Med.*, vol. 45, no. 1, pp. 53-64, Mar 2001.

[8] R. E. O'Mara, "Skeletal scanning in neoplastic disease," *Cancer*, vol. 37, no. 1 suppl, pp. 480-486, Jan 1976.

[9] R. J. Corcoran, J. H. Thrall, R. W. Kyle, R. J. Kaminski, and M. C. Johnson, "Solitary abnormalities in bone scans of patients with extraosseous malignancies," *Radiology*, vol. 121, no. 3 Pt. 1, pp. 663-667, Dec 1976.

[10] P. R. Algra, J. L. Bloem, H. Tissing, T. H. Falke, J. W. Arndt, and L. J. Verboom, "Detection of vertebral metastases: comparison between MR imaging and bone scintigraphy," *Radiographics*, vol. 11, no. 2, pp. 219-232, Mar 1991.

[11] J. A. Frank, A. Ling, N. J. Patronas, J. A. Carrasquillo, K. Horvath, A. M. Hickey, and A. J. Dwyer, "Detection of malignant bone tumors: MR imaging vs scintigraphy," *Am. J. Roentgenol.*, vol. 155, no. 5, pp. 1043-1048, Nov 1990.

[12] E. Avrahami, R. Tadmor, O. Dally, and H. Hadar, "Early MR demonstration of spinal metastases in patients with normal radiographs and CT and radionuclide bone scans," *J. Comput. Assist. Tomo.*, vol. 13, no. 4, pp. 598-602, Jul-Aug 1989.

[13] H. Bender, J. Kirst, H. Palmedo, A. Schomburg, U. Wagner, J. Ruhlmann, and H. J. Biersack, "Value of 18fluoro-deoxyglucose positron emission tomography in the staging of recurrent breast

carcinoma," *Anticancer Res.*, vol. 17, no. 3B, pp. 1687-1692, May-Jun 1997.

[14] M. Ohta, Y. Tokuda, Y. Suzuki, M. Kubota, H. Makuuchi, T. Tajima, S. Nasu, S. Yasuda, and A. Shohtsu, "Whole body PET for the evaluation of bony metastases in patients with breast cancer: comparison with <sup>99</sup>Tcm-MDP bone scintigraphy," *Nucl. Med. Commun.*, vol. 22, no. 8, pp. 875-879, Aug 2001.

[15] J. J. Peterson, M. J. Kransdorf, and M. I. O'Connor, "Diagnosis of occult bone metastases: positron emission tomography," *Clin. Orthop. Relat. R.*, no. 415 Suppl, pp. S120-128, Oct 2003.

[16] I. H. Shon and I. Fogelman, "F-18 FDG positron emission tomography and benign fractures," *Clin. Nucl. Med.*, vol. 28, no. 3, pp. 171-175, Mar 2003.

[17] J. G. Ravenel, L. L. Gordon, T. L. Pope, and C. E. Reed, "FDG-PET uptake in occult acute pelvic fracture," *Skeletal Radiol.*, vol. 33, no. 2, pp. 99-101, Feb 2004.

[18] T. Nakai, C. Okuyama, T. Kubota, K. Yamada, Y. Ushijima, K. Taniike, T. Suzuki, and T. Nishimura, "Pitfalls of FDG-PET for the diagnosis of osteoblastic bone metastases in patients with breast cancer," *Eur. J. Nucl. Med. Mol. I.*, vol. 32, no. 11, pp. 1253-1258, Nov 2005.

[19] C. S. Galasko, "Mechanisms of lytic and blastic metastatic disease of bone," *Clin. Orthop. Relat. R.*, no. 169, pp. 20-27, Sep 1982.

[20] R. H. Daffner, A. R. Lupetin, N. Dash, Z. L. Deeb, R. J. Sefczek, and R. L. Schapiro, "MRI in the detection of malignant infiltration of bone marrow," *Am. J. Roentgenol.*, vol. 146, no. 2, pp. 353-358, Feb 1986.

[21] D. K. Kido, R. Gould, F. Taati, A. Duncan, and J. Schnur, "Comparative sensitivity of CT scans, radiographs and radionuclide bone scans in detecting metastatic calvarial lesions," *Radiology*, vol. 128, no. 2, pp. 371-375, Aug 1978.

[22] A. M. Groves, C. J. Beadsmoore, H. K. Cheow, K. K. Balan, H. M. Courtney, S. Kaptoge, T. Win, S. Harish, P. W. Bearcroft, and A. K. Dixon, "Can 16-detector multislice CT exclude skeletal lesions during tumour staging? Implications for the cancer patient," *Eur. Radiol.*, vol. 16, no. 5, pp. 1066-1073, May 2006.

[23] A. Gonzalez, D. Monterrubio, M. Nequiz, R. Lopez, A. Olivos, C. Garcia de Leon, E. Tello, N. Salaiza, E. Ramos, M. Gudino, I. Montfort, and R. Perez-Tamayo, "Localization of Entamoeba histolytica amebopore in amebic liver abscesses in hamsters," *Ann. NY Acad. Sci.*, vol. 1149, pp. 375-379, Dec 2008.

[24] S. D. O'Connor, J. Yao, and R. M. Summers, "Lytic metastases in thoracolumbar spine: computer-aided detection at CT--preliminary study," *Radiology*, vol. 242, no. 3, pp. 811-816, Mar 2007.

[25] N. Otsu, "A threshold selection method from gray-level histograms," *IEEE Trans. Sys., Man and Cyber.*, vol. 9, pp. 62-66, 1979.

[26] R. M. Haralick, "Statistical and structural approaches to texture," *Proc. IEEE*, vol. 67, no. 5, pp. 786 - 804, 1979.